
Super-Resolution without High-Resolution Labels for Black Hole Simulations

Thomas Helfer

Institute for Advanced Computational Science, Stony Brook University
Stony Brook, NY 11794 USA
thomas.helfer@stonybrook.edu

Thomas D.P. Edwards

William H. Miller III Department of Physics and Astronomy, Johns Hopkins University
(currently working at Meta)
Baltimore, Maryland 21218, USA

Jessica Dafflon

Valence Labs,
6666 Rue Saint-Urbain
Montreal, QC H2S 3H1, Canada

Kaze W.K. Wong

Department of Applied Mathematics and Statistics, Johns Hopkins University
Baltimore, MD 21218, USA
Data Science and AI Institute, Johns Hopkins University
Baltimore, MD 21218, USA
Center for Computational Astrophysics, Flatiron Institute,
New York, NY 10010, USA

Matthew Lyle Olson

Intel Labs
Santa Clara CA, USA

Abstract

Generating high-resolution simulations is key for advancing our understanding of one of the universe's most violent events: Black Hole mergers. However, generating Black Hole simulations is limited by prohibitive computational costs and scalability issues, reducing the simulation's fidelity and resolution achievable within reasonable time frames and resources. In this work, we introduce a novel method that circumvents these limitations by applying a super-resolution technique *without directly needing high-resolution labels*, leveraging the Hamiltonian and momentum constraints—fundamental equations in general relativity that govern the dynamics of spacetime. We demonstrate that our method achieves a reduction in constraint violation by one to two orders of magnitude and generalizes effectively to out-of-distribution simulations.

1 Introduction

The advent of gravitational wave astronomy has started a new era in astrophysics, enabling new insights into some of the universe's most violent events, such as Black Hole mergers and neutron

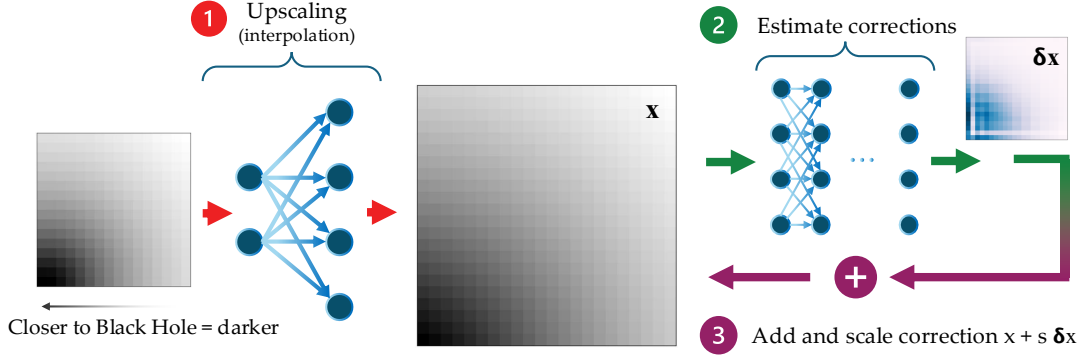


Figure 1: Schematic representation of our framework: (1) We first apply a commonly used interpolation method to up-sample our simulation, then (2) a network takes the up-sampled simulation and produces a correction δx . This correction is then (3) multiplied by the scaling factor s and added to the up-sampled simulation. The corrected simulation results in reduced constraint violations, leading to an improved simulation.

star collisions [Abbott et al., 2019, 2021, 2024, 2023]. Numerical relativity (NR) simulations play a crucial role in predicting the waveforms of such phenomena and are essential for the successful analysis of data observed by gravitational wave detectors like LIGO and Virgo [Abbott et al., 2016]. As the sensitivity of upcoming detectors (e.g., LISA Amaro-Seoane et al. [2017]) will increase by orders of magnitude, the demand for more accurate and diverse waveforms generated by NR simulations grows exponentially [Afshordi et al., 2023]. However, existing numerical methods face challenges in meeting these demands, which could limit the scientific return on the significant financial investments made in these detectors.

Next-generation detectors will require more advanced solutions capable of handling longer, higher-resolution simulations and larger mass ratios for Black Hole binaries. In this work, we present a super-resolution-inspired method that employs a convolutional neural network and uses constraints from general relativity to make the network physics-aware. The method is designed to be applied to current state-of-art numerical codes and aims to reduce simulation error and enhance the accuracy of gravitational waveform predictions.

Our framework aims to enhance adaptive mesh refinement (AMR), a widely used technique for dynamically adjusting resolution in simulations. AMR is particularly effective in situations where only specific regions, such as near black hole horizons, require higher resolution, while the rest of the simulation can operate at lower resolution. However, transitioning from low- to high-resolution grids requires the use of higher-order interpolation methods [Adams et al., 2014], which can introduce errors. To reduce these errors, we developed a super-resolution method that can be used to improve the overall accuracy of AMR simulations.

Most super-resolution techniques, however, require high-resolution labels for the training. Getting these high-resolution labels for us requires expensive simulations, and to avoid this computational cost, we propose a framework that uses a unique loss function derived from general relativity’s physical constraints. These constraints – referred to as Hamiltonian and Momentum constraints – are used for monitoring the stability of simulations. If they are not fulfilled below a threshold or show fast-growing trends, it is a strong indication of a problem in the simulation.

Another improvement brought by our framework is the ability to harness the power of parallel processing via GPUs, offering improved computational efficiency and scalability. As modern NR codebases evolve, there is a growing shift towards incorporating hardware accelerators like GPUs, in contrast to the traditionally CPU-based compute environments. This transition of NR codebases is critical, as an increasing portion of available computational resources have GPUs. Furthermore, this work demonstrates a novel application on how to leverage deep learning for numerical relativity. We believe that deep learning offers numerous opportunities to enhance NR, and when applied

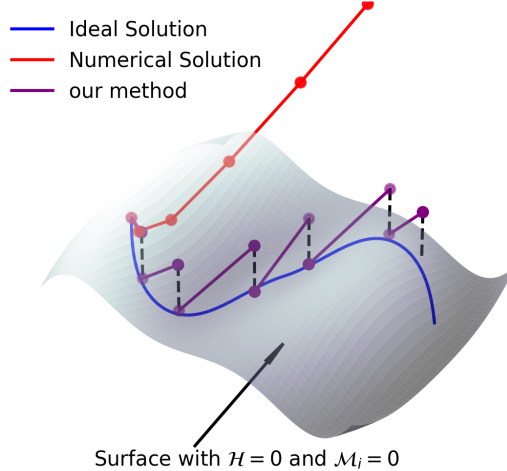


Figure 2: Visualization of the solution surface with $\mathcal{H} = 0$ and $\mathcal{M}_i = 0$. The blue line represents the ideal solution when following Einstein’s equations, while the red line illustrate a numerical solution. The dots on both the red and purple line represent the discretization of time. Our method (purple) projects the solution back to the surface where constraint are fulfilled to produce a numerical result closer to the ideal solution.

correctly, it can help close the gap in numerical performance for the next-generation gravitational wave detectors.

Our paper is organized as follows. In Section 2, we provide a brief overview of numerical relativity. In Section 3, we introduce our super-resolution framework, describing the neural network architecture, loss functions, and data generation process. In Section 4, we present our results, demonstrating the performance and generalizability of our framework, with an in-depth comparison to the L_1 loss using ground truth data. We conclude in Section 5, highlighting key results and discussing the limitations of this work.

2 Background: Numerical Relativity

Numerical relativity (NR) provides the computational framework for simulating the complex dynamics of spacetime, such as those observed in Black Hole mergers and gravitational waves. This section outlines the core concepts of numerical relativity, offering a small overview of its theoretical underpinnings. For those interested in a more in-depth exploration, please refer to Baumgarte and Shapiro [2021, 2010], Alcubierre [2008].

We work in natural units where the speed of light $c = 1$ and the gravitational constant $G_N = 1$ to simplify equations. Throughout this work, we employ Einstein summation notation, which simplifies expressions involving summations over indexed variables in tensor algebra. This notation implies that any index appearing twice in a single term is summed over. For example, the summation $C_\mu = \sum_{\nu=1}^n A_{\mu\nu} B^\nu$, where n is the number of elements of the tensor, can be written concisely using Einstein notation as $C_\mu = A_{\mu\nu} B^\nu$. Additionally, a raised index indicates summation with the inverse of the spacetime metric tensor $g_{\mu\nu}$, which we express as $g^{\mu\nu}$. For instance, $A^\mu = g^{\mu\nu} A_\nu$. When using Latin indices (i, j, k, \dots) in place of Greek indices ($\alpha, \beta, \gamma, \dots$), we employ the projected spatial metric tensor γ^{ij} to raise and lower indices in the three-dimensional spatial subspace.

2.1 Foundations of General Relativity

The theoretical backbone of NR is Einstein’s general theory of relativity [Einstein et al., 1916], which is described by the equation

$$G_{\mu\nu} = 8\pi T_{\mu\nu}. \quad (1)$$

This equation describes how matter and energy (encoded in the stress-energy tensor $T_{\mu\nu}$) influence the curvature of spacetime, represented by the Einstein tensor $G_{\mu\nu}$.

Table 1: **Simulation data** parameters used for training and test. Each simulation has multiple resolution levels, each with a different grid spacing dx . Furthermore, we give the number of boxes and how many numerical time steps the simulation performed on each level. Due to our choice of loss, we need to train a different model for each level.

resolution level	size	grid spacing dx	number of boxes	time-steps
5	263M	0.25	336	7
6	938M	0.125	1200	15
7	5.2G	0.0625	6696	31
8	19G	0.03125	24704	64
9	15G	0.015625	19208	99

The direct application of Einstein’s equations in their original form is not feasible in NR simulations due to a lack of distinction between time and space. This challenge is addressed by the Arnowitt-Deser-Misner (ADM) (3+1) decomposition [Arnowitt et al., 1959], a mathematical formalism that reformulates Einstein’s equations into a set suitable for numerical analysis. To be also numerically stable, we use the standard CCZ4 formulation [Alic et al., 2013, 2012].

Einstein’s equation in the ADM decomposition gives rise to the constraint equations that we propose for our framework as following

$$\mathcal{H} := R + \frac{2}{3}K^2 - \tilde{A}_{kl}\tilde{A}^{kl} - 16\pi\rho, \quad (2)$$

$$\mathcal{M}_i := \tilde{\gamma}^{kl} \left(\partial_k \tilde{A}_{li} - 2\tilde{\Gamma}_{l(i}^m \tilde{A}_{k)m} - 3\tilde{A}_{ik} \frac{\partial_l \chi}{2\chi} \right) - \frac{2}{3} \partial_i K - 8\pi S_i, \quad (3)$$

where R is the Ricci scalar, χ , K , \tilde{A}_{ik} and $\tilde{\gamma}^{kl}$ are evolution variables, ρ and S_i are energy and momentum density – both describe matter moving on the space manifold (e.g., Neutron Stars, Humans, Photons, cats). These equations \mathcal{H} and \mathcal{M}_i need to be equal to zero to be consistent with general relativity. However, this is never truly possible in numerical methods as the discretization introduces small errors. Although there are many methods that try to minimize this error by modifying the evolution equations (as was done in the CCZ4 formulation), with our framework, we introduce a physics-aware network to minimize these errors.

3 Methodology

Our approach combines deep learning and NR techniques to improve Black Hole simulations. We designed a super-resolution framework that applies a neural network correction to up-sampled simulations using higher order interpolation used in the GRTL code, optimizing it with a physics-aware loss based on the Hamiltonian and Momentum constraints of general relativity. By performing small correction to enforce constraints, we aim to achieve a more accurate simulation as depicted in Fig. 2. The code used for training and evaluation is available at <https://github.com/ThomasHelfer/TorchGRTL>. The higher order interpolation is separately available at <https://github.com/ThomasHelfer/PyInterpX> and via `pip install pyinterpX`.

3.1 Loss functions

In contrast to supervised ML methods – where we would use the distance between predicted and ground truth as a loss – here we use the sum of squares of the violation of Eq. 2 and Eq. 3.

$$\mathcal{L}_{\text{GR}} = \sum_j \left(|\mathcal{H}(\mathbf{x}_j)|^2 + \sum_{i=0}^D |\mathcal{M}_i(\mathbf{x}_j)|^2 \right), \quad (4)$$

where D is the number of spatial dimensions (three for our experiments) and \mathbf{x}_j represent positions on the simulation grid. We defined the normalized loss to evaluate the performance of our model and the baseline obtained by the higher order interpolator currently used in some NR codes as

$$\text{Normalized } \mathcal{L}_{\text{GR}} = \frac{\mathcal{L}_{\text{GR}}(\text{Our method})}{\mathcal{L}_{\text{GR}}(\text{Baseline})}. \quad (5)$$

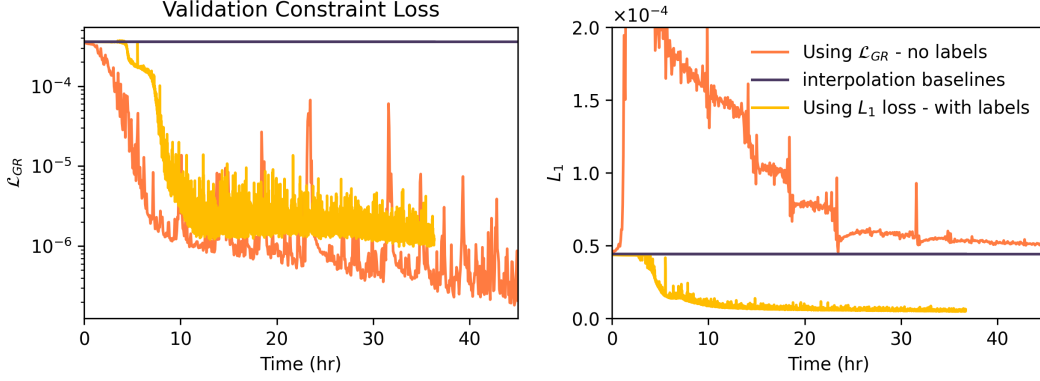


Figure 3: Comparing the performance of models trained with L_1 loss (which requires high-resolution labels) and \mathcal{L}_{GR} loss (which does not require high-resolution labels). As shown in the left figure, both L_1 and \mathcal{L}_{GR} losses converge to similarly small values of \mathcal{L}_{GR} . However, in the right figure, we observe that both \mathcal{L}_{GR} and L_1 converge to different values of L_1 . This suggests that the two losses lead to different solutions, likely due to the under-specified nature of the constraint-based \mathcal{L}_{GR} loss. The dark straight line is the interpolation used in GRTL code.

3.2 Dataset generation

Our framework employs GRTeclyn (formerly GRChombo [Radia et al., 2022, Andrade et al., 2021]) an established open-source codebase for the NR simulations. We simulate two equal-mass Black Holes in a quasi-circular orbit¹, a common reference benchmark in numerical relativity (similar to how the MNIST dataset is used as a benchmark in computer vision).

To be able to fit our simulations in GPU memory we subdivided them into blocks of $(16 \times 16 \times 16)$ points and 25 channels representing different evolution variables (i.e., χ , K , \tilde{A}_{ik} , $\tilde{\gamma}_{kl}$, α and β^i). We trained on 80% of the data and used 20% to test the in-distribution performance. To test out-of-distribution performance, we also created several independent simulations with increasing Black Hole masses² (See Table 3 for details).

In our adaptive mesh simulations, we work with multiple resolution levels, each generating data at different rates. Due to the nature of our loss function, we need to train separate models for each resolution level. Notably, the amount of data varies between these levels, ranging from 263 MB to 19 GB (See Table 1). The highest resolution levels typically generate the most data because our simulation uses subcycling, where higher levels undergo more time steps relative to the lower levels.

3.3 Framework architecture

An overview of the framework architecture can be found in Fig. 1. First we up-sample our simulation from low resolutions using a higher order interpolator commonly used throughout Black Holes simulations [Schnetter et al., 2004]. The upsampled simulations will not only be the input for the neural network that calculates the correction δx , but also serve as the baseline. As we do not know the scale of the correction a priori, we introduce a rescale factor s to reduce floating-point problems. So, our correction is

$$x + s\delta x, \quad (6)$$

where x is the vector of all variables $x = (\chi, K, \tilde{A}_{ik}, \dots)$ and for our data, we found that $s = 10^{-4}$ or 10^{-5} works well.

Numerical Stability As the Hamiltonian and Momentum constraints (Eq. 2 and 3) are mathematically underspecified (we have 25 variables and only four equations), there are many possible solutions

¹Data is available at <https://huggingface.co/datasets/thelfer/BinaryBlackHole>.

²Data is available at <https://huggingface.co/datasets/thelfer/BinaryBlackHoleValidation>

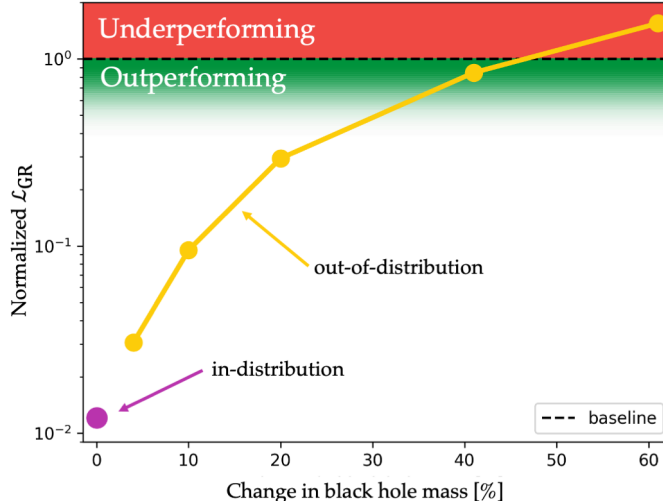


Figure 4: **Our framework (purple and yellow) outperforms the baseline (dotted black) by two orders of magnitude.** In NR simulations, the mass of a Black Hole is a parameter for defining the simulation. We evaluate the loss of the validation set in the in-distribution scenario (purple). However, we aimed to stress-test our framework by varying the Black Hole’s mass, enabling us to *evaluate its ability to generalize to out-of-distribution scenarios* (yellow). Remarkably, even with a 41% variation in the Black Hole’s mass, our framework still outperforms the baseline. A more complete overview can be found in Tabel 2.

that the system can take. We can address this by introducing masking, changing our correction (Eq. 6) at training to

$$x + m \cdot s\delta x, \quad (7)$$

where m is a mask. We found that a mask where every fourth element in each direction is masked, with a random shift applied, performed best in guiding the solution compared to a fully random mask.

To clarify the effectiveness of this approach, consider a scenario where δx is large. When comparing two neighboring points, if one is masked while the other is not, there is a significant difference between them. This difference leads to large gradients, which increases the \mathcal{L}_{GR} loss. As a result, solutions with large δx are penalized. By encouraging smaller values of δx , we keep the corrected simulation close to its original state x .

To gain further insights into potential solutions within our framework, we conducted experiments by down-sampling boxes with $16 \times 16 \times 16$ resolution down to $8 \times 8 \times 8$, allowing us to establish a clear ground truth for evaluating our up-sampling methods. To maintain comparability, we aligned the interpolation grid such that every second element is directly copied from the low-resolution data (see Fig. 7), while the other elements are determined through interpolation.

Neural Network Details Since translation symmetry is inherently encoded in Einstein’s gravity when using a Cartesian grid, convolutional neural networks are a natural choice for our framework. We constructed a convolutional neural network composed of 4 hidden layers with 64 channels and ReLU non-linearity at the end of every hidden layer. To keep both input and output sizes the same, we employ padding. Lastly, as the gradients involved in this process can be very small, we use double precision to avoid any underflow issues.

4 Results

Our framework improves simulation quality by one to two orders of magnitude, as measured by our loss \mathcal{L}_{GR} , with performance varying based on the specific data and model. It also generalizes well to out-of-distribution simulations, as shown in Fig. 3.3 and Table 2 for a comprehensive overview. The important contribution of our paper is the introduction of the physics-aware loss \mathcal{L}_{GR} , because of it our approach does not need any high resolution labels, making the data generation significantly

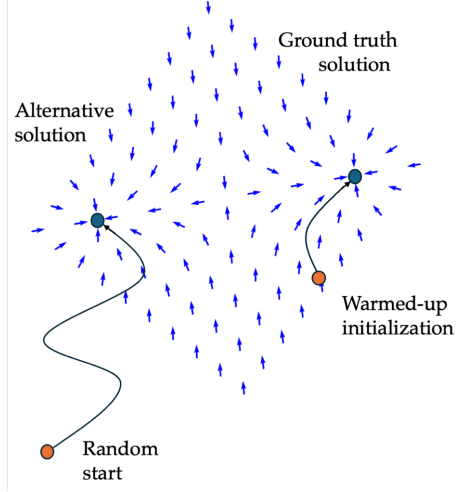


Figure 5: **Multiple solutions:** Depending on starting point, we can control what state our simulations falls into when using the \mathcal{L}_{GR} loss. When we start with a pre-trained network (marked as Warmed-up initialization), we can converge towards the ground truth.

cheaper. While the \mathcal{L}_{GR} loss incurs a higher computational cost per iteration compared to the L_1 , it converges significantly faster. In our experiments, the slower per-iteration time is roughly balanced by fewer required iterations, resulting in similar overall convergence times compared to L_1 (See Fig. 3).

There are two ways to use the presented framework (see Table 2). The first, as discussed so far, is to correct errors introduced by the interpolation routine in adaptive mesh refinement. The second approach involves maintaining the original resolution of the simulation and using the framework to correct numerical errors that accumulate during the simulation. This second use case extends the framework’s applicability beyond adaptive mesh refinement. By applying it directly to fixed-resolution or single-resolution simulations, our method can enhance simulations on any mesh. This capability is particularly valuable for improving the accuracy of complex simulations prone to constraint buildup, such as those in modified gravity scenarios or simulations of highly spinning black holes.

4.1 Multiple Solutions and how to control them

In this section, we compare the results of training with the L_1 loss versus the \mathcal{L}_{GR} loss. In Fig. 3 (left), we observe that training with the L_1 loss also minimizes \mathcal{L}_{GR} , which is expected since the ground truth approximately satisfies the \mathcal{L}_{GR} constraints. However, Fig. 3 (right) shows that training with the \mathcal{L}_{GR} loss versus the L_1 loss leads to different solutions. When trained with the \mathcal{L}_{GR} loss, the model converges to a solution close to the interpolation baseline. In contrast, training with the L_1 loss produces a solution closer to 0, indicating alignment with the ground truth. These differences in solutions are due to the under-specified nature of the \mathcal{L}_{GR} loss, which allows for multiple solutions that satisfy the constraints but are distinct from the ground truth.

It is also possible to achieve convergence to the ground truth solution without directly using the L_1 loss (as depicted in Fig. 5). This is based on the observation that the ground truth solution found by L_1 is, at least approximately, also a solution for \mathcal{L}_{GR} . By initializing closer to the desired solution, we can improve convergence to that solution under \mathcal{L}_{GR} . To demonstrate this, we took a network already trained with L_1 loss and resumed training using \mathcal{L}_{GR} on a different simulation, where the mass differed by roughly 20% relative to the initial simulation used for L_1 training. We refer to this as the ‘warmed-up’ solution. We observed that this differently initialized network converged to a state with a small \mathcal{L}_1 value (See Fig. 6). However, if the difference in mass becomes too large, we are no longer able to achieve this convergence.

In this paper, we do not claim that one solution is inherently preferable for numerical simulations. However, if a solution close to the ground truth is desired, our experiments suggest that a combination of training strategies can help achieve this without fully relying on high-resolution labels. Unlike

Table 2: **The normalized loss** of models in our GitHub repository (<https://github.com/ThomasHelfer/TorchGRTL/tree/main/models>). The column “config-name” corresponds to the folder name in the repository, “factor” specifies the upscaling factor applied to the simulation, and “level” indicates the resolution level at which the model was trained. A factor of 1 corresponds to the use case where the framework is applied at the original simulation resolution to correct accumulated numerical errors, while factors of 2 and 4 represent the use case where the framework corrects errors introduced by the interpolation routine. For better visualization, we plotted data from the model “x1-lvl9” in Fig. 3.3. Lastly, $\Delta M = 0$ represents the test set from the training simulation, while other values of ΔM indicate our out-of-distribution datasets.

config-name	factor	level	change in Black Hole mass $\Delta M \rightarrow$					
			0%	4%	10%	20%	41%	61%
x1-lvl5	1	5	0.172	0.090	0.090	0.100	0.205	2.078
x1-lvl6	1	6	0.067	0.183	0.234	0.427	1.361	4.570
x1-lvl7	1	7	0.144	0.166	0.228	0.488	1.971	5.378
x1-lvl9	1	9	0.012	0.030	0.095	0.295	0.844	1.549
x2-lvl5	2	5	0.150	0.232	0.420	1.345	5.838	15.154
x2-lvl6	2	6	0.060	0.148	0.312	1.129	6.140	19.088
x2-lvl7	2	7	0.077	0.121	0.324	1.242	7.280	23.514
x2-lvl8	2	8	0.158	0.187	0.326	1.019	4.450	13.110
x2-lvl9	2	9	0.231	0.326	0.749	1.483	2.608	5.771
x4-lvl5	4	5	0.585	0.546	0.612	0.764	1.390	2.383

typical foundation models, which often involve pre-training on large unlabeled datasets followed by fine-tuning on labeled data, we propose a reverse approach: pre-training on a small labeled dataset with L_1 loss, followed by post-training on a larger, cheaper unlabeled dataset using \mathcal{L}_{GR} loss.

4.2 Related work

It is important to draw a clear distinction between Physical Informed Neural Networks (PINNs Raissi et al. [2017]), which also use partial differential equations (PDEs) as a loss. While our framework takes an approximation of the solution as input and uses the physical constraints to improve it, PINNs take the spatial coordinates and produce the value of the PDE solution at the given coordinate. Furthermore, while PINNs need to be retrained for each new simulation, our method needs to be trained once and can then be inferred on different simulations.

4.3 Limitations

Despite the improvements that our method brings, there are three main limitations that could improve the impact of our analysis. Firstly, our analysis is conducted offline, our framework is applied only after the simulation has finished. Ideally, our framework would be applied online, replacing the baseline interpolation within an adaptive mesh codebase. However, implementing an online approach presents additional challenges, such as the engineering effort required to integrate our method with a NR codebase. These hurdles will be addressed in future research. Secondly, the trained neural network depends on the grid spacing (dx). Therefore, to operate across the varying spacings present in an adaptive mesh solver, with our current methods training a separate network for each resolution would be required. Thirdly, we are not fully using all available symmetries in our system. We expect that including equivariance with respect rotational symmetries [Gregory et al., 2023] would result in reduced need of training data.

5 Conclusion

In this work, we tested the applicability of deep learning techniques to numerical relativity simulations. We demonstrated that by introducing a physics-aware loss, we enable solutions without high-resolution labels, or, if a ground truth solution is preferred, require only a small amount of

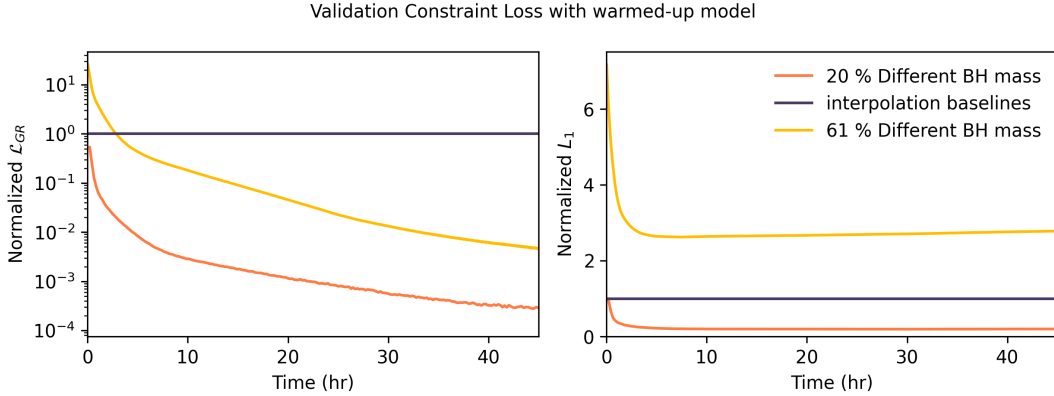


Figure 6: The effect of using a warmed-up model. In this figure, we use a network pre-trained with a supervised L_1 loss and fine-tune it using the \mathcal{L}_{GR} loss on a different dataset. This is done on two datasets: one where the binary black hole mass differs by 20% and another where it differs by 61%. Both cases show convergence in \mathcal{L}_{GR} (in the left figure). The first (with 20% mass difference) approaches zero in normalized L_1 (right figure), indicating that the \mathcal{L}_{GR} loss can converge toward the ground truth if initialized properly. However, the 61 % network is too different and thus does not converge close to the ground truth.

high-resolution data to guide the network. This significantly reduces reliance on computationally expensive data.

Acknowledgments and Disclosure of Funding

Research reported in this publication was supported by a Postdoctoral Fellowship at the Institute for Advanced Computational Science, Stony Brook University. This work was carried out at the Advanced Research Computing at Hopkins (ARCH) core facility (rockfish.jhu.edu), which is supported by the National Science Foundation (NSF) grant number OAC1920103. The Flatiron Institute is a division of the Simons Foundation.

References

- B. P. Abbott et al. GW151226: Observation of Gravitational Waves from a 22-Solar-Mass Binary Black Hole Coalescence. *Phys. Rev. Lett.*, 116(24):241103, 2016. doi: 10.1103/PhysRevLett.116.241103.
- B. P. Abbott et al. GWTC-1: A Gravitational-Wave Transient Catalog of Compact Binary Mergers Observed by LIGO and Virgo during the First and Second Observing Runs. *Phys. Rev. X*, 9(3):031040, 2019. doi: 10.1103/PhysRevX.9.031040.
- R. Abbott et al. GWTC-2: Compact Binary Coalescences Observed by LIGO and Virgo During the First Half of the Third Observing Run. *Phys. Rev. X*, 11:021053, 2021. doi: 10.1103/PhysRevX.11.021053.
- R. Abbott et al. GWTC-3: Compact Binary Coalescences Observed by LIGO and Virgo during the Second Part of the Third Observing Run. *Phys. Rev. X*, 13(4):041039, 2023. doi: 10.1103/PhysRevX.13.041039.
- R. Abbott et al. GWTC-2.1: Deep extended catalog of compact binary coalescences observed by LIGO and Virgo during the first half of the third observing run. *Phys. Rev. D*, 109(2):022001, 2024. doi: 10.1103/PhysRevD.109.022001.
- Mark F. Adams, Phillip Colella, Daniel T. Graves, Jeffrey N. Johnson, Hans Johansen, Noel Keen, Terry J. Ligocki, Daniel F. Martin, Peter McCorquodale, David Modiano, Peter O. Schwartz,

- T. D. Sternberg, and Brian van Straalen. Chombo software package for amr applications design document. 2014. URL <https://api.semanticscholar.org/CorpusID:59810615>.
- Niaesh Afshordi et al. Waveform Modelling for the Laser Interferometer Space Antenna. 11 2023.
- Miguel Alcubierre. *Introduction to 3+ 1 numerical relativity*, volume 140. OUP Oxford, 2008.
- Daniela Alic, Carles Bona-Casas, Carles Bona, Luciano Rezzolla, and Carlos Palenzuela. Conformal and covariant formulation of the z4 system with constraint-violation damping. *Phys. Rev. D*, 85: 064040, Mar 2012. doi: 10.1103/PhysRevD.85.064040. URL <https://link.aps.org/doi/10.1103/PhysRevD.85.064040>.
- Daniela Alic, Wolfgang Kastaun, and Luciano Rezzolla. Constraint damping of the conformal and covariant formulation of the z4 system in simulations of binary neutron stars. *Phys. Rev. D*, 88: 064049, Sep 2013. doi: 10.1103/PhysRevD.88.064049. URL <https://link.aps.org/doi/10.1103/PhysRevD.88.064049>.
- Pau Amaro-Seoane, Heather Audley, Stanislav Babak, John Baker, Enrico Barausse, Peter Bender, Emanuele Berti, Pierre Binetruy, Michael Born, Daniele Bortoluzzi, Jordan Camp, Chiara Caprini, Vitor Cardoso, Monica Colpi, John Conklin, Neil Cornish, Curt Cutler, Karsten Danzmann, Rita Dolesi, Luigi Ferraioli, Valerio Ferroni, Ewan Fitzsimons, Jonathan Gair, Lluis Gesa Bote, Domenico Giardini, Ferran Gibert, Catia Grigani, Hubert Halloin, Gerhard Heinzl, Thomas Hertog, Martin Hewitson, Kelly Holley-Bockelmann, Daniel Hollington, Mauro Hueller, Henri Inchauspe, Philippe Jetzer, Nikos Karnesis, Christian Killow, Antoine Klein, Bill Klipstein, Natalia Korsakova, Shane L Larson, Jeffrey Livas, Ivan Lloro, Nary Man, Davor Mance, Joseph Martino, Ignacio Mateos, Kirk McKenzie, Sean T McWilliams, Cole Miller, Guido Mueller, Germano Nardini, Gijs Nelemans, Miquel Nofrarias, Antoine Petiteau, Paolo Pivato, Eric Plagnol, Ed Porter, Jens Reiche, David Robertson, Norma Robertson, Elena Rossi, Giuliana Russano, Bernard Schutz, Alberto Sesana, David Shoemaker, Jacob Slutsky, Carlos F. Sopuerta, Tim Sumner, Nicola Tamanini, Ira Thorpe, Michael Troebis, Michele Vallisneri, Alberto Vecchio, Daniele Vetrugno, Stefano Vitale, Marta Volonteri, Gudrun Wanner, Harry Ward, Peter Wass, William Weber, John Ziemer, and Peter Zweifel. Laser interferometer space antenna. 2017. URL <https://arxiv.org/abs/1702.00786>.
- Tomas Andrade et al. GRChombo: An adaptable numerical relativity code for fundamental physics. *J. Open Source Softw.*, 6(68):3703, 2021. doi: 10.21105/joss.03703.
- R. Arnowitt, S. Deser, and C. W. Misner. Dynamical structure and definition of energy in general relativity. *Phys. Rev.*, 116:1322–1330, Dec 1959. doi: 10.1103/PhysRev.116.1322. URL <https://link.aps.org/doi/10.1103/PhysRev.116.1322>.
- Thomas W Baumgarte and Stuart L Shapiro. *Numerical relativity: solving Einstein's equations on the computer*. Cambridge University Press, 2010.
- Thomas W Baumgarte and Stuart L Shapiro. *Numerical relativity: starting from scratch*. Cambridge University Press, 2021.
- Albert Einstein et al. The foundation of the general theory of relativity. *Annalen Phys*, 49(7):769–822, 1916.
- Wilson Gregory, David W. Hogg, Ben Blum-Smith, Maria Teresa Arias, Kaze W. K. Wong, and Soledad Villar. Geometricimagnet: Extending convolutional neural networks to vector and tensor images, 2023. URL <https://arxiv.org/abs/2305.12585>.
- Miren Radia, Ulrich Sperhake, Amelia Drew, Katy Clough, Pau Figueras, Eugene A. Lim, Justin L. Ripley, Josu C. Aurrekoetxea, Tiago França, and Thomas Helfer. Lessons for adaptive mesh refinement in numerical relativity. *Class. Quant. Grav.*, 39(13):135006, 2022. doi: 10.1088/1361-6382/ac6fa9.
- Maziar Raissi, Paris Perdikaris, and George Em Karniadakis. Physics informed deep learning (part i): Data-driven solutions of nonlinear partial differential equations. *arXiv preprint arXiv:1711.10561*, 2017.
- Erik Schnetter, Scott H. Hawley, and Ian Hawke. Evolutions in 3-D numerical relativity using fixed mesh refinement. *Class. Quant. Grav.*, 21:1465–1488, 2004. doi: 10.1088/0264-9381/21/6/014.

Table 3: Summary of masses of Black Holes in the binary simulation generated for training and out-of-distribution (OOD) performance evaluation. The table lists corresponding Black Hole masses (M) and percentage increases (ΔM) relative to the training mass.

Black Hole Mass M	ΔM	used for
0.4884	0	training
0.5084	4%	OOD
0.5384	10%	OOD
0.5884	20%	OOD
0.6884	41%	OOD
0.7884	61%	OOD

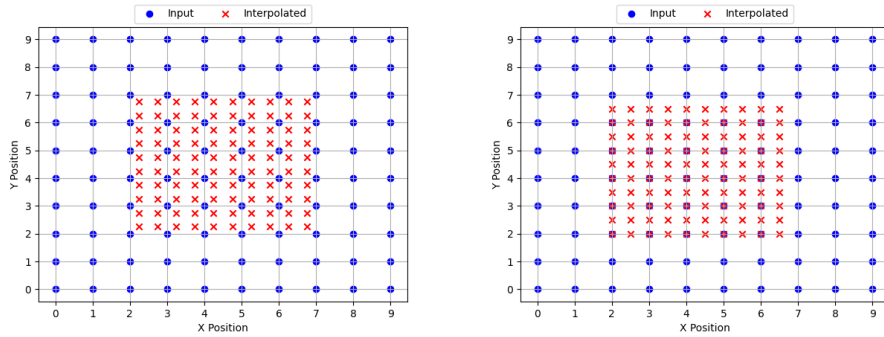


Figure 7: Different grid alignments are used throughout the paper for interpolation. The blue points represent the low-resolution grid, while the red points correspond to the high-resolution interpolation grid. The left image shows the alignment used in the GRTEclyn code, which is applied to all models in Table 2. The image on the right demonstrates the alignment chosen for the experiment in Section 3.3, where downsampling is simplified by selecting every second element.